



A novel defect-based fatigue damage model coupled with an optimized neural network for high-cycle fatigue analysis of casting alloys with surface defect

Tongzhou Gao^a, Chenhao Ji^a, Zhixin Zhan^{a,*}, Yingying Huang^a, Chuanqi Liu^b, Weiping Hu^a, Qingchun Meng^a

^a School of Aeronautic Science and Engineering, Beihang University, Beijing 100191, China

^b State Key Laboratory of Nonlinear Mechanics, Institute of Mechanics, Chinese Academy of Sciences, Beijing 100090, China

ARTICLE INFO

Keywords:

High-cycle fatigue
Casting alloys
Surface defect
Damage model
Optimized neural network

ABSTRACT

A novel defect-based fatigue damage model coupled with an optimized neural network is proposed for high-cycle fatigue prediction. Based on parametric studies and continuum damage mechanics, the defect-based fatigue damage evolution equation is derived, and the numerical simulation and fatigue damage computation are then implemented and validated. After that, more computations are performed to acquire a batch of reliable fatigue data, and the database is obtained. Finally, the architecture of the optimized neural network is established, and the predicted results are verified by experimental fatigue data. The proposed methodology works well for the fatigue analysis of casting alloys with surface defect.

1. Introduction

As two commonly used casting alloys, ZL114A alloy has excellent casting properties, high specific strength, and good fatigue resistance, while ZM6 alloy has a light specific gravity, high specific stiffness, and excellent creep resistance. They are widely employed in military, aerospace, transportation and other fields. However, during assembly, a number of defects (including scratches and impact pits) tend to develop on the surface of the casting alloys, which obviously affect fatigue properties and induce a greater risk to the safety and reliability of the structure in engineering applications. Therefore, it is necessary to investigate the high-cycle fatigue behaviour and an effective approach for life prediction of casting alloys.

A comprehensive literature review shows that the commonly-used fatigue analysis methods include the critical plane, energy density, damage mechanics, field measurement, probabilistic statistics, molecular dynamics, phase field, peridynamics, and machine learning. These methods have their advantages and are widely employed in engineering applications. The notch critical plane approach is adopted to predict the fatigue life of metallic notched test pieces [1], and the crack initiation and propagation prediction of fatigue damage region [2]. The strain energy density-based fatigue criterion is developed to predict the

multiaxial fatigue life prediction of metals [3] and study the effects of mean stress on uniaxial fatigue behavior [4]. The damage mechanics-based method is adopted to study the influence of overload on notch fatigue behavior [5] and simulate the fatigue dispersion in duplex microstructure titanium alloys [6]. The low-cycle fatigue evaluation of welded joints is carried out using the DIC-based strain approach [7–8]. The probabilistic approach is used to estimate the fatigue life of notched components under size effects [9] and the fatigue life of adhesively bonded joints [10]. The molecular dynamics simulation is conducted to analyse the micro-structural aspects of fatigue crack propagation [11] and the fatigue behaviour of pre-cracked aluminium chip for NEMS application [12]. The phase-field method is employed to model the crack nucleation and propagation of rubber [13], and the fracture and fatigue in shape memory alloys [14]. Liu et al. [15] built a fatigue damage-cumulative model in peridynamics to study the fatigue crack growth rates. Nguyen et al. [16] developed an energy-based peridynamic model to simulate fatigue cracking. The machine learning based approach is investigated in-depth to research the fatigue behaviour of additively manufactured metals [17] and predict the rate-dependent multiaxial fatigue behaviour of polyamide-6 [18].

It is reported that most studies are focused on the effects of casting defects, porosity, and microstructure on the fatigue behaviour of casting

* Corresponding author.

E-mail address: zxxupe@163.com (Z. Zhan).

<https://doi.org/10.1016/j.ijfatigue.2023.107538>

Received 1 November 2022; Received in revised form 17 January 2023; Accepted 19 January 2023

Available online 24 January 2023

0142-1123/© 2023 Elsevier Ltd. All rights reserved.

alloys. In terms of casting defects, Couper et al. [19] studied the casting defects and the fatigue behaviour of an aluminium casting alloy, indicating that the fatigue life could be predicted based on the size of the casting defects. The casting defects and fatigue strength were compared between standard specimens and production components [20]. Serrano-Munoz et al. [21] analysed the effects of surface and internal casting defects on fatigue properties. With regard to porosity, the influence of porosity on the fatigue limit of cast alloys was studied by Mayer et al. [22], and the scatter in fatigue life was mainly due to the porosity in cast aluminium–silicon alloys [23]. The experimental study of porosity by Buffiere et al. [24] found that the fatigue life and the lifetime scatter depended on the pore content, especially at high-stress level. Concerning microstructure, Siegfanz et al. [25] investigated the influence of microstructure on the fatigue damage behaviour of cast alloys, revealing that the fatigue crack propagation behaviour was closely related to the morphology of the solid solution/eutectic microstructure. The relationship was established between microstructure characteristics and the fatigue parameters of casting alloy [26].

In recent years, machine learning methods, as a more efficient and accurate method, have been widely used in engineering, especially in predicting mechanical properties. Machine learning-based models (ANN, SVR, and RF) are implemented to study the effect of defect/inclusion on fatigue behavior in steels [27], predict finite fatigue life in metal materials containing defects [28], correlate defect features and fatigue life of 17–4 PH stainless steel [29] and analyze the fatigue scattering and assessment of 300 M–AerMet100 steel [30]. Investigations of fatigue uncertainty are also conducted, including the fatigue uncertainty estimation of Ni-based superalloy by SVR [31], fatigue uncertainty quantification of composite materials by ANN [32], probabilistic fatigue evaluation of joints in orthotropic steel decks by the dynamic Bayesian network [33], and probabilistic creep-fatigue damage assessment by machine learning models [34]. Furthermore, the material fatigue problems in advanced additive manufacturing are also widely analyzed using machine learning methods, such as the very-high-cycle fatigue life prediction of Ti-6Al-4V alloy fabricated by selective laser melting [35], fatigue assessment of post-processed additively manufactured AlSi10Mg [36], fatigue analysis of metal additive manufacturing considering effects of build orientation and post-processing [37], and the fatigue life prediction for laser-directed energy deposition titanium alloys [38].

In this work, a novel defect-based fatigue damage model coupled with an optimized neural network is proposed for high-cycle fatigue prediction of casting alloys with surface defect. The entire paper is organized as below. In Section 2, the experimental studies, including the preparation of ZL114A and ZM6 specimens and the experimental fatigue results, are briefly described. In Section 3, the formulation of the defect-based fatigue damage model and the calibration of material parameters is carried out. Section 4 presents the numerical implementation, fatigue damage computation, and validation of the proposed theoretical model. Finally, in Section 5, the architecture of the optimized neural network model is established, and the model training and predicted results are obtained.

2. Experiments

2.1. Preparation of ZL114A and ZM6 specimens

The standard smooth specimens in Fig. 1 are directly manufactured from ZL114A and ZM6 blanks. For scratch defects, a tooling with a circular surface is first designed, and a standard specimen is placed on the tooling. The large circular surface on one side of the specimen must be kept in line with the surface of the tooling. Second, the specimen is fixed on the numerical control machine using a clamping device, and a tool with a cutter radius of 0.2 mm is employed. The tool is controlled to move parallel to the thickness direction of the specimen, and the tool position is adjusted to achieve different depths of scratches. As listed in

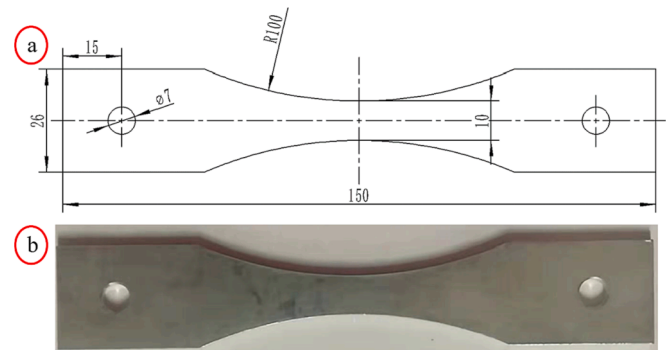


Fig. 1. (a) Geometrical dimension of smooth specimen (all dimensions in mm) and (b) fatigue test specimen.

Table 1
Defect sizes of ZL114A and ZM6 specimens.

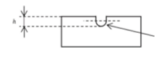
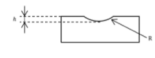
Type of defect	Radius/mm	Depth/mm	Kt
 Scratch	0.2	0.15	2.48
		0.25	2.97
		0.35	3.36
 Impact pit	3	0.15	1.34
		0.25	1.43
		0.35	1.50

Table 1, the specimens with three kinds of the scratch defects in Fig. 2(a) are manufactured. For impact pit defects, a punch with a radius of 3 mm is used to obtain the desired impact depth by controlling the downward displacement of the punch. After punching one side, the specimen is switched up and down, and the crater on the other side is fabricated using the same procedure. Finally, the geometry of the crater is measured to meet the machining accuracy requirements. Table 1 lists three kinds of specimens with impact depth, and Fig. 2(b) shows the experimental specimen with the impact pit.

2.2. Fatigue experiments of ZL114A and ZM6 specimens

Based on the test standard of HB 5287–96 [39], the fatigue experiments of ZL114A and ZM6 specimens are conducted on the QBG-100CC resonant high-frequency fatigue machine. The test loading frequency is between 110 Hz and 130 Hz, and the specific loading frequency is related to the specimen size. The load control is used, the number of cyclic loads is recorded, and the criterion for fatigue failure of the specimen is a 5 Hz reduction in test frequency. This criterion is adopted because the resonant frequency of the equipment decreases if a fatigue crack appears in the specimen. A fatigue crack initiates when the frequency is reduced by about 5 Hz.

In order to better understand the fatigue behavior of ZL114A and ZM6 materials, fatigue experiments are conducted under loading conditions, and further fracture analyses are performed on the specimens. Smooth specimens are tested at different stress ratios ($R = 0.02, 0.5$) with the maximum stresses ranging from 120 MPa to 250 MPa in one loading cycle. In addition, the fatigue experiments of specimens with scratch and impact pit are carried out with the stress ratio of $R = 0.02$, and the maximum stress ranges in a loading cycle from 90 MPa to 230 MPa, and 110 MPa to 200 MPa, respectively.

Fig. 3 is plotted for the fatigue data of ZL114A and ZM6 specimens. It is observed that the dispersion of the fatigue data of ZM6 alloy is larger than that of ZL114A alloy, which may be related to the defects inside the test specimens. To gain more insight into the fatigue dispersion of ZM6 alloy, the scanning electron microscope (SEM) analysis is performed on the fracture surfaces of several selected specimens, as shown in Figs. 4–6. Fig. 4 shows the fracture surface of the ZM6 smooth specimen observed

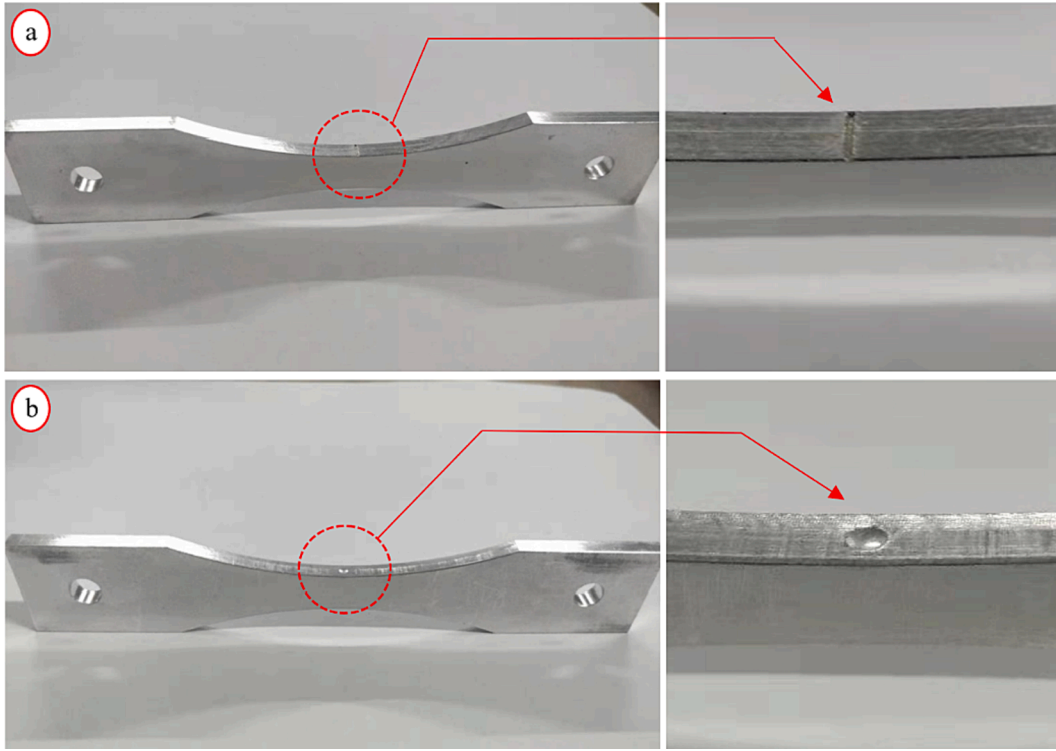


Fig. 2. (a) The specimen with scratch and (b) the specimen with impact pit.

at $R = 0.02$, and we can clearly observe the black inclusions in Fig. 4 (a) and the holes in Fig. 4 (b), which are formed during the manufacturing process and result in poor fatigue performance. Fig. 5 is plotted for the fracture surface of the ZM6 scratched specimen under the loading condition of $R = 0.02$ and $\sigma_{\max} = 95$ MPa. It is noted that although the fatigue cracks in the ZM6 scratched specimens initiate from the holes, there is a significant difference in their lifetimes at the same stress level. The hole in Fig. 5(b) is closer to the boundary of the specimen than the hole in Fig. 5(a), so the fatigue crack is more likely to occur and has a shorter life. The fracture surface of the ZM6 pitted specimen with $R = 0.02$ and $\sigma_{\max} = 120$ MPa is presented in Fig. 6, from which we can clearly observe that multiple fatigue cracks initiate at large inclusions. The crack initiation region, stable crack extension region, and rapid fracture region can be seen clearly in the fracture morphology of the three types of post-mortem specimens. It is found that the crack initiation sites of all specimens are located on the surface or near the surface defects of larger volume. For the scratched specimens, the crack initiation defect is located at the cross-section where the scratch is located. In contrast, for the pitted specimens, the crack initiation defect is located at the cross-section where the impact pit is located. Thus, surface and internal defects affect the onset and development of fatigue cracking in the specimens. According to the above analysis, it is concluded that the casting process could induce inclusions and holes within the ZM6 alloy. At the same time, the size, shape, and location of defects have an important impact on fatigue behavior, leading to a significant dispersion of the experimental fatigue data.

3. Formulation of the defect-based fatigue damage model

3.1. Damage coupled constitutive model

In the continuum damage mechanics (CDM) [41], damage refers to the generation and development of micropores and microcracks. These microscopic defects are discontinuous, but a continuity assumption can be made in CDM, i.e., the effect of microscopic defects on material properties can be characterized by one or several continuous internal

field variables/damage variables. For the representative volume element (RVE) of an isotropic material, the damage degree in a given direction is defined as the ratio of the defect cross-sectional area to the total cross-sectional area,

$$D = \frac{S_D}{S} \quad (1)$$

where D represents the damage degree, S is the total cross-sectional area, and S_D is the defective cross-sectional area. When $D = 0$, the material is undamaged; when $D = 1$, the material is completely damaged and loses its load-bearing capacity, which means fatigue cracks are generated. The effective bearing area S_R of the RVE is then obtained,

$$S_R = (1 - D)S \quad (2)$$

The effective stress $\tilde{\sigma}$ is defined as,

$$\tilde{\sigma} = \frac{\sigma}{1 - D} \quad (3)$$

where σ is the nominal stress. It is noted that the effective stress characterizes the effect of damage on the internal stress of the material.

Since the stress concentration caused by defects could lead to elasto-plastic deformation near the scratch and pit, a nonlinear elasto-plastic constitutive model is employed for analysis. In the case of small strains, the total metal strain can be divided into elastic and plastic strains,

$$\varepsilon_{ij} = \varepsilon_{ij}^e + \varepsilon_{ij}^p \quad (4)$$

where ε_{ij}^e is the elastic strain and ε_{ij}^p is the plastic strain. In this case, the elastic strain with damage is obtained based on the strain equivalence assumption [42]:

$$\varepsilon_{ij}^e = \frac{1 + \nu}{E} \left(\frac{\sigma_{ij}}{1 - D} \right) - \frac{\nu}{E} \left(\frac{\sigma_{kk}}{1 - D} \right) \delta_{ij} \quad (5)$$

where E is the modulus of elasticity, ν is the Poisson's ratio, and σ_{ij} is the stress component. $\delta_{ij} = \begin{cases} 0, & i \neq j \\ 1, & i = j \end{cases}, (i = 1, 2, 3; j = 1, 2, 3).$

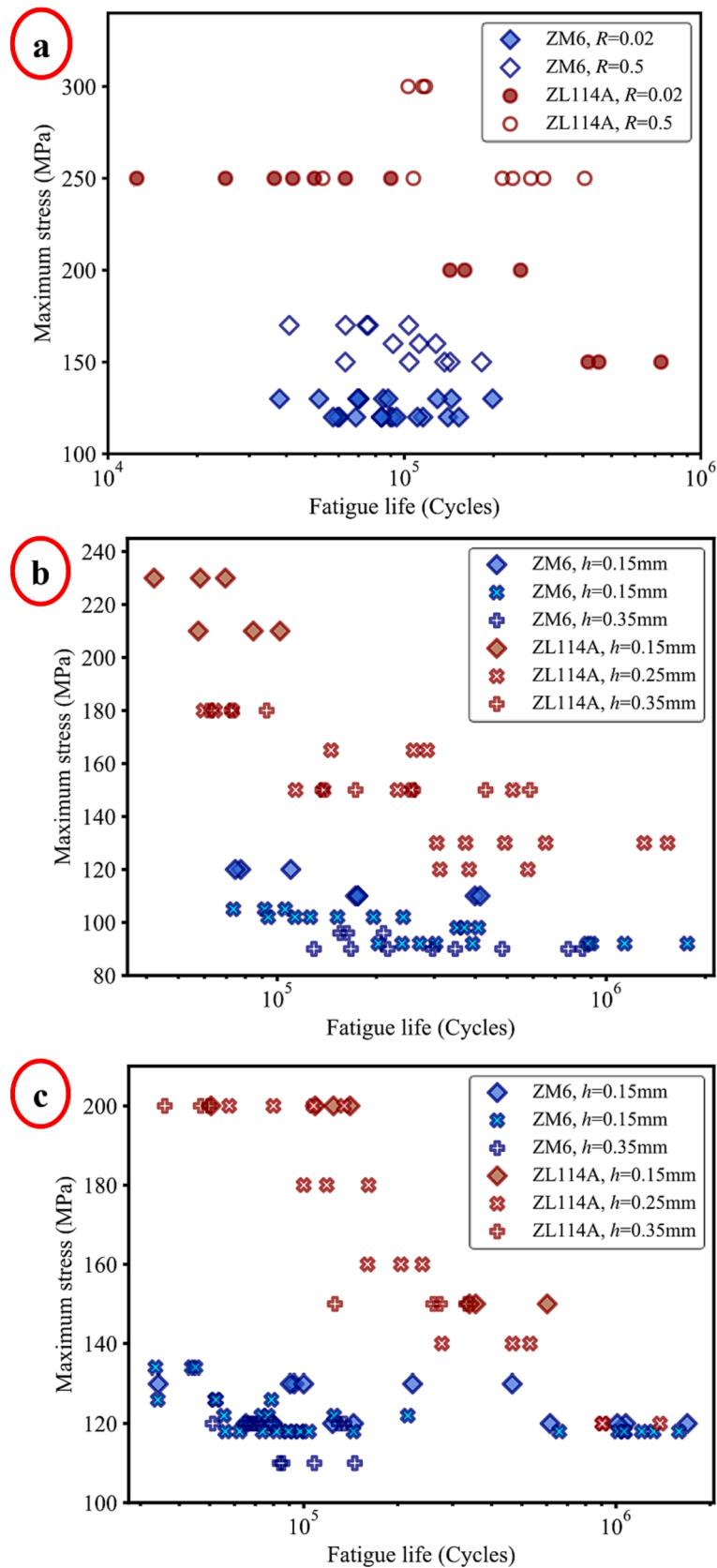


Fig. 3. The fatigue results for the ZL114A [40] and ZM6 specimens: (a) $R = 0.02$ and $R = 0.5$ for the smooth specimens, (b) $R = 0.02$ for the specimens with scratch, and (c) $R = 0.02$ for the specimens with impact pit.

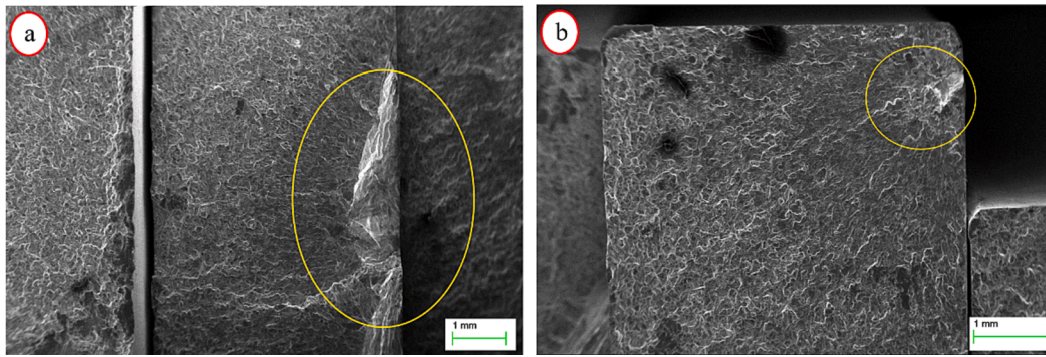


Fig. 4. The fracture surface of the ZM6 smooth specimen: (a) $R = 0.02$, $\sigma_{\max} = 120$ MPa, $N_f = 8,300$; (b) $R = 0.02$, $\sigma_{\max} = 130$ MPa, $N_f = 37,900$.

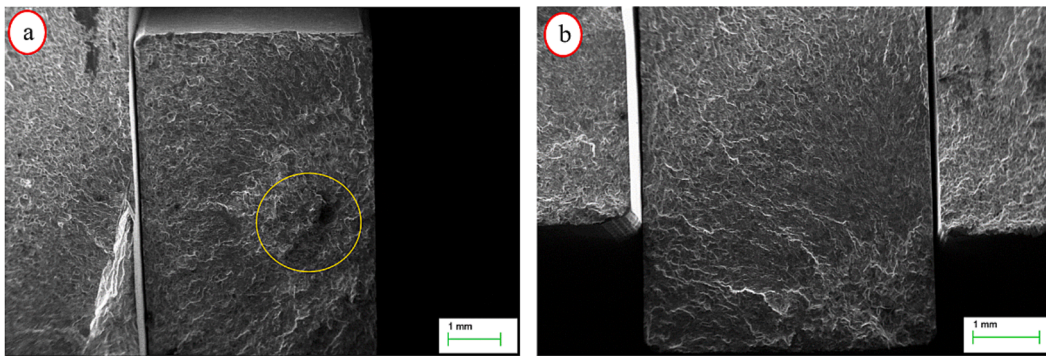


Fig. 5. The fracture surface of the ZM6 scratched specimen: (a) $R = 0.02$, $\sigma_{\max} = 95$ MPa, $N_f = 538,100$; (b) $R = 0.02$, $\sigma_{\max} = 95$ MPa, $N_f = 139,200$.

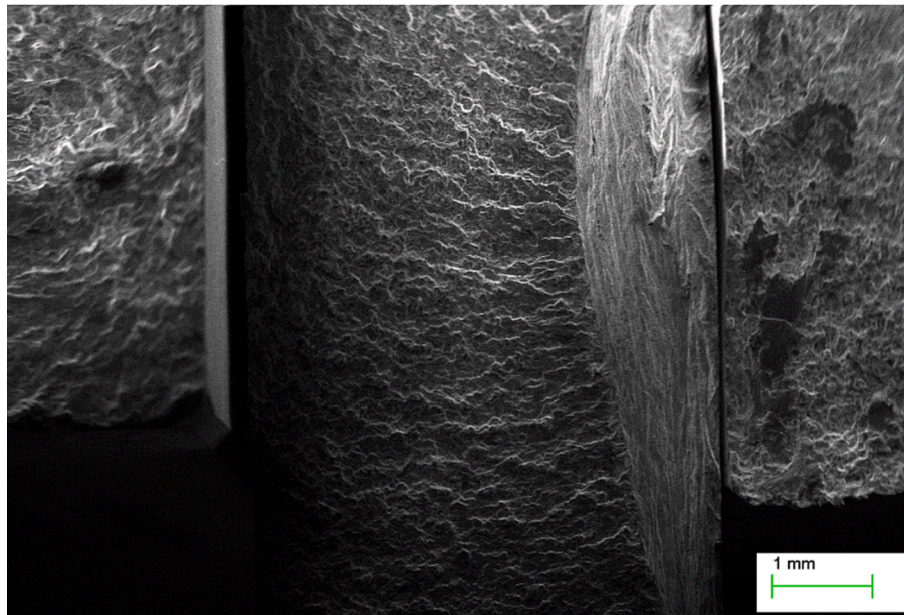


Fig. 6. The fracture surface of the ZM6 pitted specimen with $R = 0.02$, $\sigma_{\max} = 120$ MPa, $N_f = 5,600$.

In this case, the yield function coupled with damage and the plastic flow criterion is expressed below [43],

$$F = \left(\frac{\sigma_{ij}}{1-D} - \alpha_{ij} \right)_{eq} - \sigma_y \quad (6)$$

$$\dot{\epsilon}_{ij}^p = \dot{\lambda} \frac{\partial F}{\partial \sigma_{ij}} = \frac{3}{2} \frac{\dot{\lambda}}{1-D} \frac{(\frac{\sigma_{ij}}{1-D} - \alpha_{kl})_{dev}}{(\frac{\sigma_{ij}}{1-D} - \alpha_{kl})_{eq}} \quad (7)$$

$$\dot{p} = \sqrt{\frac{2}{3} \dot{\epsilon}_{ij}^p \dot{\epsilon}_{ij}^p} = \frac{\dot{\lambda}}{1-D} \quad (8)$$

where eq represents the von Mises equivalent stress, dev represents the bias part of the stress, α_{ij} is the back stress, σ_y represents the yield stress, $\dot{\lambda}$ is the plastic multiplier, and \dot{p} is the cumulative plastic strain rate. The hardening equation coupled with damage is

$$\alpha_{ij} = \sum_{k=1}^K \alpha_{ij}^{(k)} \quad (9)$$

$$\dot{\alpha}_{ij}^{(k)} = (1-D) \left(\frac{2}{3} C_k \dot{\epsilon}_{ij}^p - \gamma_k \alpha_{ij}^{(k)} \dot{p} \right) \quad (10)$$

where K is the number of back stress components, and C_k and γ_k are the material parameters calibrated from the test data.

3.2. Fatigue damage model development

3.2.1. CDM-based fatigue damage model (Model-1)

For the case of uniaxial high cycle fatigue, the fatigue damage evolution model [44] is shown below

$$\dot{D} = \frac{dD}{dN_f} = a \left(\frac{\sigma_a}{1 - n\sigma_m} \right)^m (1-D)^{-\beta} \quad (11)$$

where σ_a represents the stress amplitude, and σ_m . a , β , m , and n are the materials parameters to be calibrated.

For the case of multiaxial high-cycle fatigue, the fatigue damage evolution model is

$$\dot{D} = \frac{dD}{dN_f} = a \left(\frac{\sigma_a^*}{1 - n\sigma_m^*} \right)^m (1-D)^{-\beta} \quad (12)$$

where σ^* represents the damage equivalent stress.

$$\sigma^*(\sigma_{ij}) = \sigma_{eq} \left[\frac{2}{3}(1+\nu) + 3(1-2\nu) \left(\frac{\sigma_H}{\sigma_{eq}} \right)^2 \right]^{\frac{1}{2}} \quad (13)$$

$$\sigma_a^* = \frac{1}{2} \sigma^*(\sigma_{max} - \sigma_{min}) \quad (14)$$

$$\sigma_m^* = \frac{1}{2} \sigma^*(\sigma_{max} + \sigma_{min}) \quad (15)$$

where σ_H is the hydrostatic stress, σ_{eq} is the equivalent stress, and ν is the Poisson's ratio. σ_{max} represents the maximum stress, and σ_{min} the minimum stress. By integrating the Eq. (11) from $D = 0$ to $D = 1$, we obtain

$$N_f = \frac{1}{a(1+\beta)} \left(\frac{\sigma_a}{1 - n\sigma_m} \right)^{-\beta} \quad (16)$$

where N_f is the number of loading cycles for crack initiation.

3.2.2. Defect-based fatigue damage model (Model-2)

(1) Definition of defect impact factor (DIF).

It is generally known that pits and scratches are two typical surface defects of metal structures. The effect of defects on fatigue can be attributed to the stress concentration caused by the defects. The stress concentration coefficient increases with the increase of hole diameter and increases with the decrease of hole depth. Therefore, it is necessary to focus on the stress concentration caused by surface defect, i.e., the defect impact factor (DIF) in this study. The ratio of the peak stress to the nominal stress in the net section is defined as the DIF. Therefore, this subsection first investigates the relationship curve between the typical size of the defect and the DIF.

In the case of plate specimens, the radius and depth of the defect along the width direction are very critical. In the geometric configuration of scratches and pits, the geometry of the defect can be completely defined by obtaining the values of the depth h and the radius r . Parametric finite element (FE) analysis based on the COMSOL platform is thus performed to investigate the relationship between the DIF and defect dimensions. The depth h and radius r are dimensionless parameters, and the axial stress is set to 100 MPa. The FE mesh is automatically divided into quadrilateral meshes, and the mesh around the defect is automatically updated as the defect size parameters change, provided

that convergence and calculation accuracy are satisfied.

The parametric FE results are shown in Figs. 7 and 8 for the specimen with the defect size of $h = 0.25$ mm and $r = 0.2$ mm. It is seen that the maximum stress value of 297 MPa for the scratch and 143 MPa for the pit are approximately-two and three times the loading load, indicating that the defect causes stress concentration. The variations of DIF with the depth h and the radius r are shown in Fig. 9, and we can see that the deeper the depth and the larger the radius of the scratch and pit, the larger the DIF. Furthermore, we also investigate the variation of DIF with the ratio $R_{h/r}$ of the depth h and the radius r . As plotted in Fig. 10, the variation pattern of the DIF with $R_{h/r}$ is the same for different radii and depths, and the DIF grows faster when $R_{h/r}$ is less than 0.3 and slower when it exceeds 0.3. Based on the above analysis, the relationship between the DIF and $R_{h/r}$ is proposed as below

$$DIF = a(R_{h/r})^b + c \quad (17)$$

The parameters $a = 1.541$, $b = 0.6712$, and $c = 1.128$ are calibrated by the least square method. Fig. 11 is plotted for the fitted DIF - $R_{h/r}$ curve.

(2) The novel fatigue damage model.

It is known that the surface defect at the edge of the specimen is an important factor affecting the fatigue life and crack initiation location. The larger the DIF caused by a scratch or a pit, the more likely a crack will initiate. Therefore, the DIF is introduced into the stress-related term of the damage evolution equation. The defect-based fatigue damage model is proposed as below

$$\begin{cases} \dot{D} = \frac{dD}{dN_f} = a \left[\frac{DIF^p \sigma_a}{(1 - nDIF^p \sigma_m)(1-D)} \right]^\beta, \text{for uniaxial fatigue} \\ \dot{D} = \frac{dD}{dN_f} = a \left[\frac{DIF^p \sigma_a^*}{(1 - nDIF^p \sigma_m^*)(1-D)} \right]^m, \text{for multiaxial fatigue} \end{cases} \quad (18)$$

where p is a material parameter related to material and defect type. The terms $DIF^p \sigma_a$ and $DIF^p \sigma_m$ reflect the effect of stress concentration caused by defects on fatigue damage.

$$\begin{cases} N_f = \frac{1}{a(1+\beta)} \left(\frac{DIF^p \sigma_a}{1 - nDIF^p \sigma_m} \right)^{-\beta}, \text{for uniaxial fatigue} \\ N_f = \frac{1}{a(1+\beta)} \left(\frac{DIF^p \sigma_a^*}{1 - nDIF^p \sigma_m^*} \right)^{-\beta}, \text{for multiaxial fatigue} \end{cases} \quad (19)$$

It is worth noting that both surface defects and internal microstructural defects affect fatigue life. In this study, we focus on the effect of surface defects on fatigue life, and the DIF is completely defined in terms of the geometric parameters of the surface defects. The influence of internal microstructural defects on fatigue life is indirectly reflected by the material parameters of the fatigue damage model. The fatigue life of casting alloys with the surface defects can be predicted by the predictive model. Furthermore, the DIF should mainly affect the fatigue damage of the material around the surface defect. When the shape and size of the defect and the applied fatigue loads are given, the fatigue life of the specimen could be accurately computed by using the proposed fatigue damage model. On the one hand, the fatigue damage of the material far from the defect is small and has little effect on the fatigue life of the specimen. On the other hand, we are more concerned about the fatigue damage of the local material around the defect. Therefore, the proposed fatigue damage model works for the fatigue life prediction of the specimen with a defect and the fatigue damage computation of material around the defect.

3.3. Material parameters calibration

Two types of material parameters need to be calibrated. For the material parameters in the damage-coupled constitutive model, C_k and γ_k are obtained by fitting the relationship between the stress and strain using the static tensile test data, as shown below. Table 2 lists the

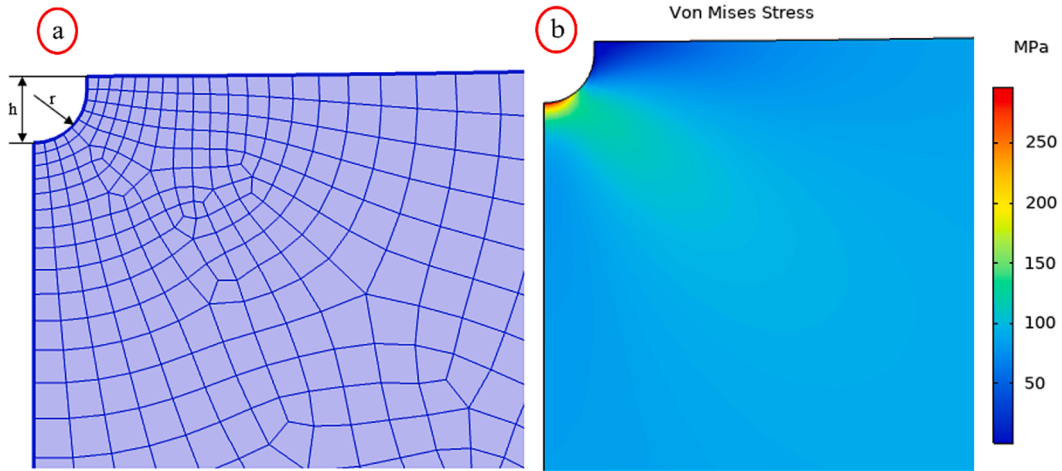


Fig. 7. (a) FE model for the specimen with scratch, and (b) the parametric FE result.

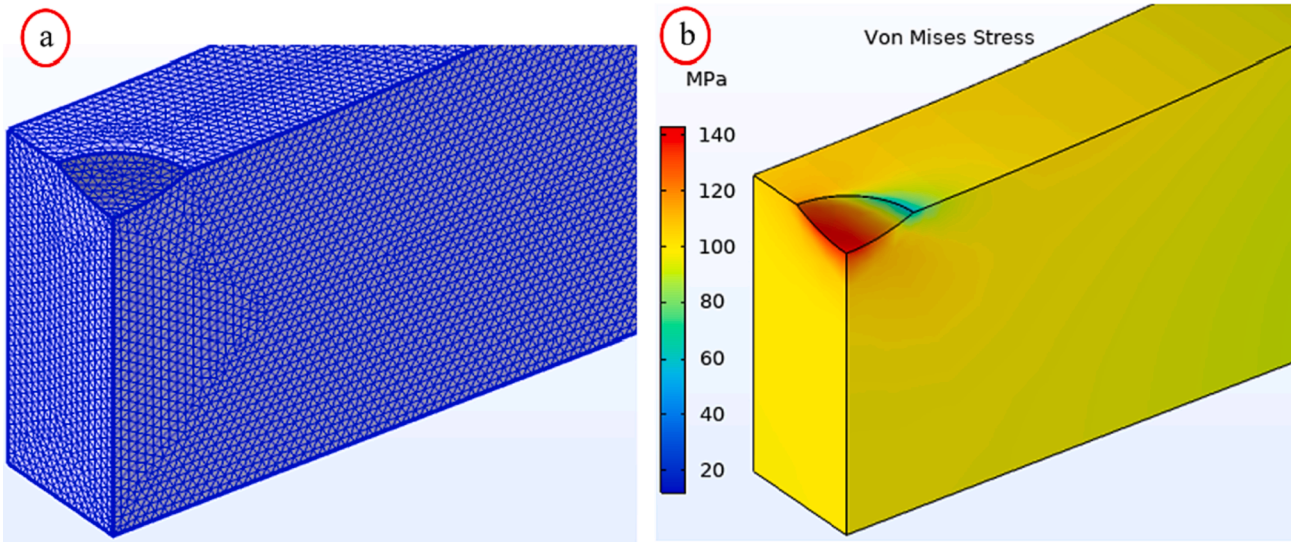


Fig. 8. (a) FE model for the specimen with impact pit, and (b) the parametric FE result.

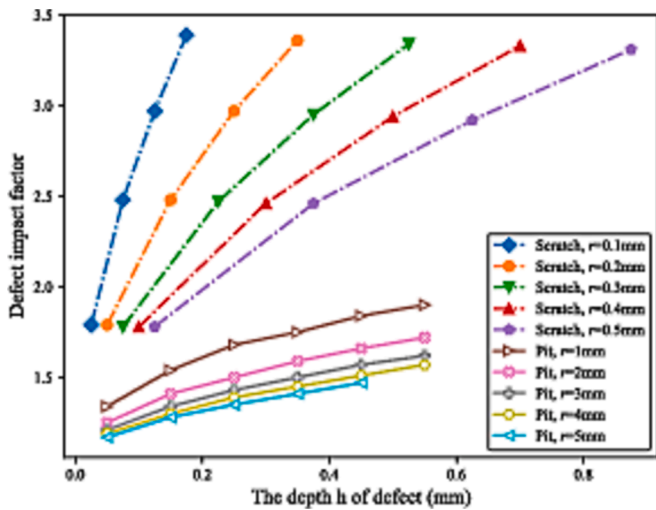


Fig. 9. Variations of *DIF* with the depth *h* and the radius *r*.

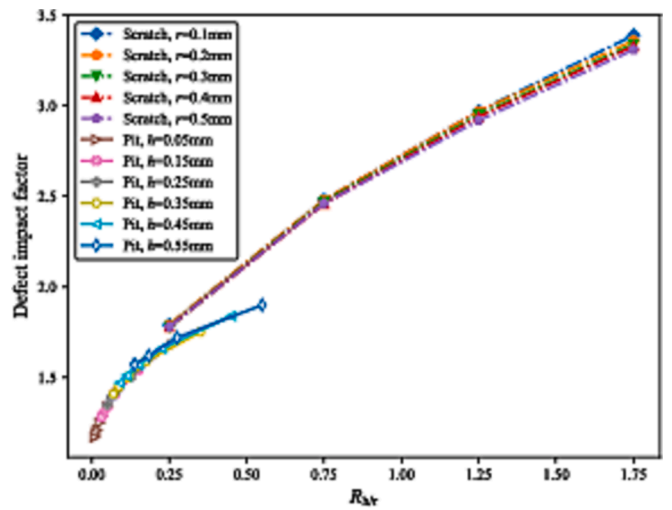


Fig. 10. Variations of *DIF* with the ratio $R_{h/r}$ of the depth *h* and the radius *r*.

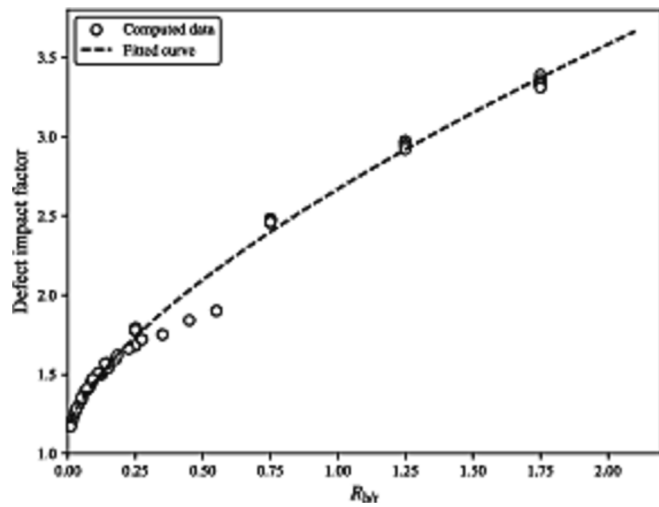


Fig. 11. The fitted $DIF - R_{h/r}$ curve for the specimens with scratch and impact pit.

calibrated parameter, and the stress–strain curves for the ZL114A and ZM6 alloys are plotted in Fig. 12. It is noted that it's better to calibrate the kinematic hardening parameters using the cyclic stress–strain curve from the reversed loading tests. In this work, the cyclic stress–strain curves of ZL114A and ZM6 alloys are not measured, and the monotonic tensile test data are employed to calibrate these parameters by the least squares method. In general, the cyclic stress–strain curve of aluminum alloy differs from the monotonic tensile stress–strain curve in the plastic or hardening stage. However, they basically coincide exactly in the elastic stage. This work aims to carry out high-cycle fatigue analysis, in which the elastic damage dominates the damage evolution of the material. Therefore, the calibrated parameters are reliable for high-cycle fatigue life predictions under cyclic loading conditions.

$$\sigma = \sum_{k=1}^K \frac{C_k}{\gamma_k} (1 - e^{-\gamma_k \epsilon_p}) + \sigma_y \quad (20)$$

In terms of the material parameters in the defect-based fatigue damage model, there are four parameters, a , β , n , and p that need to be calibrated. First, based on the fatigue test data of smooth specimens, the material parameters a , β , and n are fitted using the least squares method, and the calibrated results are shown in Table 3. After that, parameter p is calibrated by comparing the predicted results with the experimental data of the notched specimens. The least square method is used to fit the parameter p . The MAPE (mean absolute error percentage) is chosen as an index to judge the fitting effect, as shown in Eq. (21), where x_t is experimental data, and x_t^{pre} is predicted data. The physical meaning of the MAPE is the average of the percentage errors of the predicted and actual values for each data set. The smaller the MAPE, the better the fit. Fig. 13 is plotted for the variation of the MAPE versus the parameter p , and all the calibrated results are shown in Table 3. Furthermore, the computed MAPE for Model-1 and Model-2 are listed in Table 4, and the calibrated results are shown in Fig. 14. It can be seen that most of the results obtained by Model-2 fall within the twice error band, and only two points of the ZM6 scratched specimens fall between the twice and triple error band. It is noted that the proposed defect-based fatigue damage model is not very general, considering that the parameters are

Table 2
Material parameters in the damage-coupled constitutive model.

Material	E/MPa	ν	σ_y/MPa	C_1	C_2	C_3	γ_1	γ_2	γ_3
ZL114A	72,700	0.3	210	13935.2	31607.2	14276.4	1056.2	471.4	964.7
ZM6	43,400	0.3	142	1748.9	2880.5	1343.7	169.8	70.4	8.2

related to the defect geometry of the specimen. Nevertheless, the form of the proposed model and the method of material parameters calibration can be referred to predict the fatigue life of materials with other defects.

$$MAPE = \sum_{t=1}^n \left| \frac{x_t - x_t^{pre}}{x_t} \right| \times \frac{100}{n} \quad (21)$$

4. Numerical computation of fatigue life based on the defect-based fatigue damage model

4.1. Numerical implementation

In this study, the FE numerical computation is implemented on the Abaqus platform, a commonly-used software suite for complex FE analysis and computer-aided engineering. This section presents the numerical method to implement the damage-coupled constitutive model and defect-based fatigue damage model. The secondary development is performed by the UMAT subroutine, in which the user-defined material constitutive model and fatigue damage model are implemented. The coupled computation of the stress and damage field is also realized. The computational flowchart is briefly presented as below: (1) Initialize all parameters, and the initial values of the current integration point variables are passed to UMAT; (2) Compute the stresses and strains for each loading step based on the damage coupled elastoplastic constitutive equations and the current damage degree; (3) According to the current stress field, compute the current damage increment from the damage evolution equation and update the damage degree, then return to the main ABAQUS program; (4) Repeat the above steps until the damage degree is 1. At this point, the crack is considered to initiate, and the number of cycles to failure is obtained.

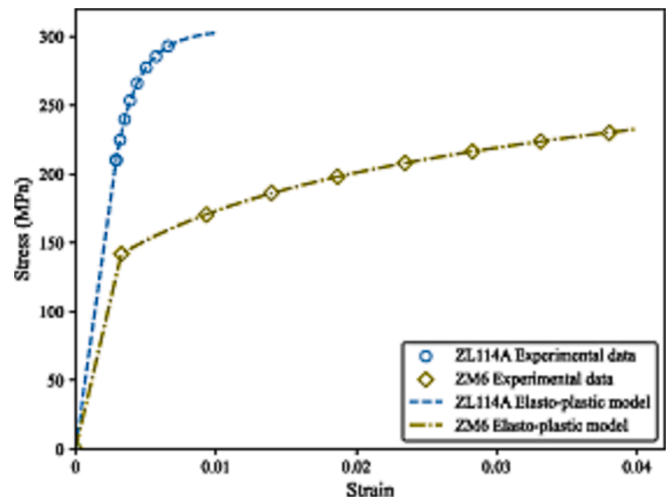


Fig. 12. The stress–strain curve for ZL114A and ZM6 alloys.

Table 3
Material parameters in the defect-based fatigue damage model.

Material	α	β	n	$p(\text{for pit})$	$p(\text{for scratch})$
ZL114A	8.89×10^{-13}	2.936	0.002455	0.52	0.212
ZM6	1.40×10^{-9}	1.815	0.003966	0.222	-0.014

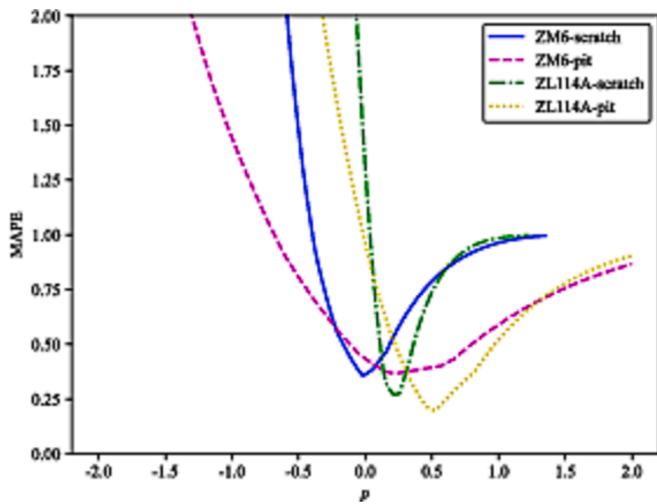


Fig. 13. Variation of the MAPE versus the parameter p .

Table 4

The computed MAPE for Model-1 and Model-2.

Type	MAPE by Model-1	MAPE by Model-2
ZL114A with impact pit	99.83 %	19.8096 %
ZL114A with scratch	134.1741 %	27.5528 %
ZM6 with impact pit	35.8547 %	26.1863 %
ZM6 with scratch	32.1226 %	31.445 %

4.2. FE model

Due to the symmetry of the specimen, a 1/4 model is established for FE analysis to save computational time, and the symmetric displacement constraints are applied on the symmetry surface. For cyclic loading, the tensile stress is applied at the outer end of the specimen. The field outputs are set to stress, strain, and damage degree. In addition, mesh convergence verification is also performed. The local mesh refinement is

performed at the smallest section of the smooth and defected specimens to ensure that the stress remains consistent, and the good mesh convergence is achieved. The C3D8 element is adopted. A total of 26,248 nodes and 19,282 elements are used to mesh the smooth specimen, 32,629 nodes and 24,304 elements are used to mesh the scratched specimen, and 31,352 nodes and 23,725 elements are used to mesh the impacted specimen. The FE model of the smooth specimen is shown in Fig. 15.

4.3. Fatigue life computation by the fatigue model

4.3.1. Computed results for the smooth specimens

For the ZL114A smooth specimen, the distribution of the damage field under the fatigue loads of $R = 0.5$ and $S_{max} = 250MPa$ is shown in Fig. 16. It can be seen that the stress is highest at the minimum cross-sectional area of the specimen, which is also the initiation point of fatigue cracking. The distribution patterns of the damage and stress fields are basically the same. Fig. 17(a) is plotted for the variation of stress versus the number of loading cycles, and the stress of the dangerous element gradually decreases with the increase of the number of cycles. The trend of damage degree with the number of loading cycles is shown in Fig. 17(b). It is noted that the damage grows slowly in the first 85 % and 90 % of the lifetime, while the damage increases sharply, and the crack initiates faster in the last 10 % of the lifetime.

For the ZM6 smooth specimen under the fatigue loads of $R = 0.02$ and $S_{max} = 130MPa$, the distribution of the damage field and the variations of the stress and damage degree versus the number of cycles have similar patterns, as shown in Figs. 18 and 19. The numerically predicted results are compared with the experimental results of the ZL114A and ZM6 smooth specimens under different fatigue loads, as shown in Fig. 20. It is found that all the predicted fatigue lives are within the twice error band, indicating that the calibrated material parameters have good accuracy and can be employed to compute the fatigue lives of specimens with scratch and impact pit.

4.3.2. Computed results for the specimen with scratch and pit

For the specimen with scratch, Fig. 21(a) is plotted for the compared results between the numerically computed fatigue lives and the

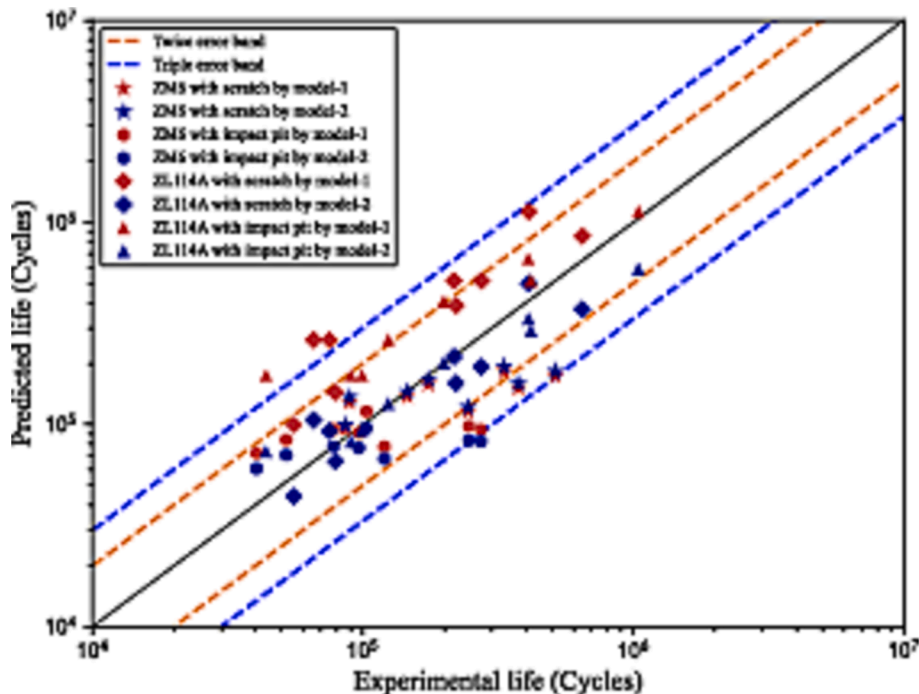


Fig. 14. The calibrated results of Model-1 and Model-2.

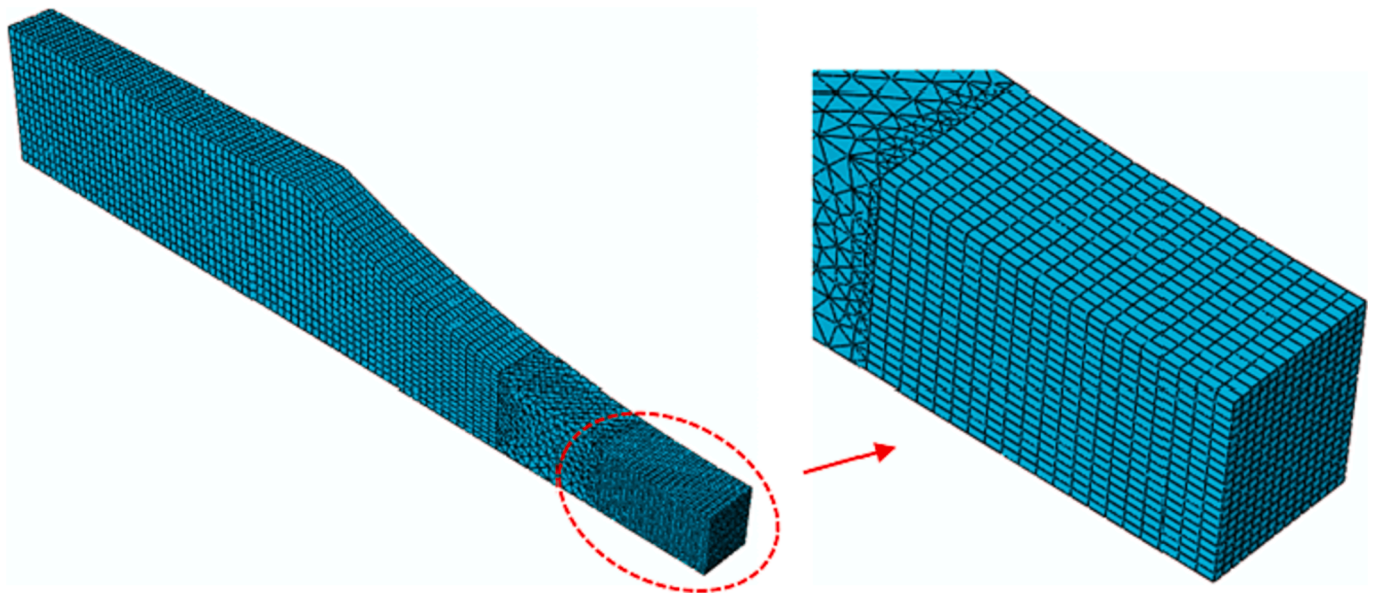


Fig. 15. The model of smooth specimen.

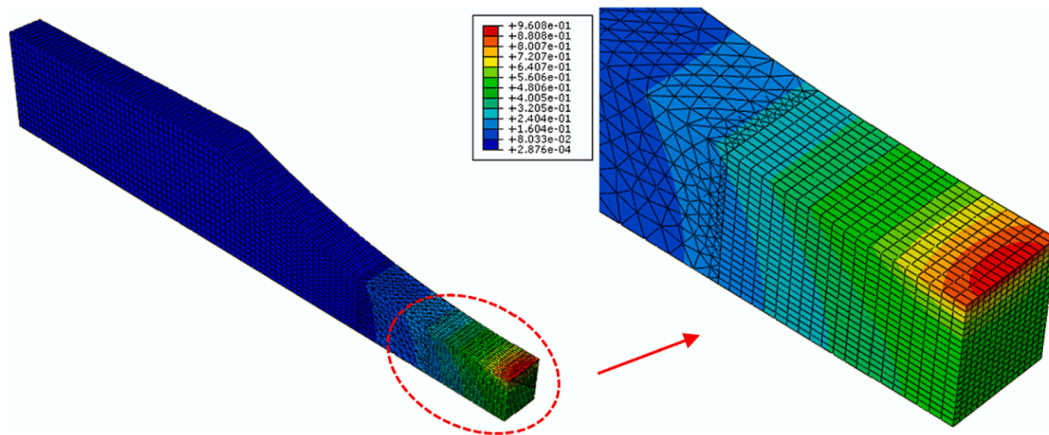


Fig. 16. Damage distribution of the ZL114A smooth specimen with $R = 0.5$ and $S_{max} = 250\text{MPa}$.

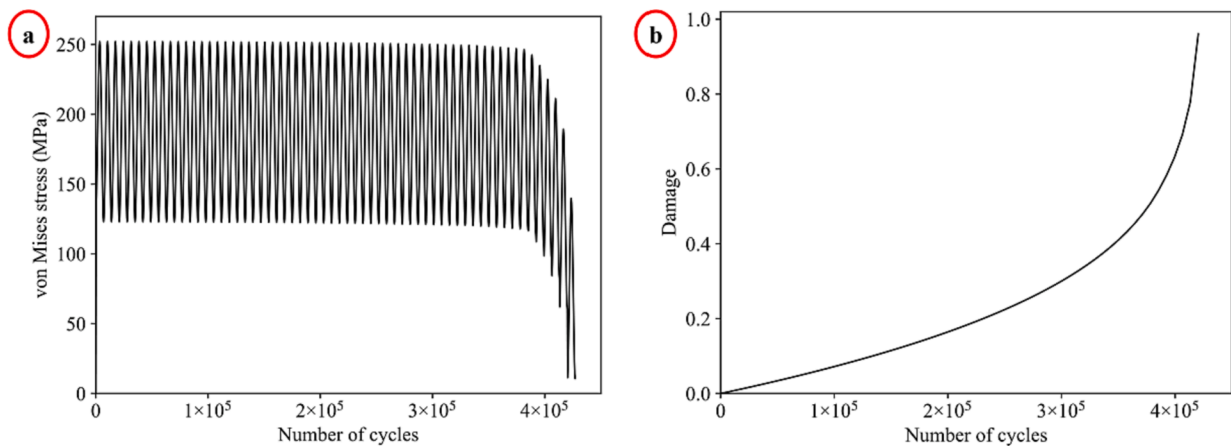


Fig. 17. For the ZL114A smooth specimen with $R = 0.5$ and $S_{max} = 250\text{MPa}$, (a) variation of von Mises stress versus the loading cycles, and (b) variation of damage versus the loading cycles.

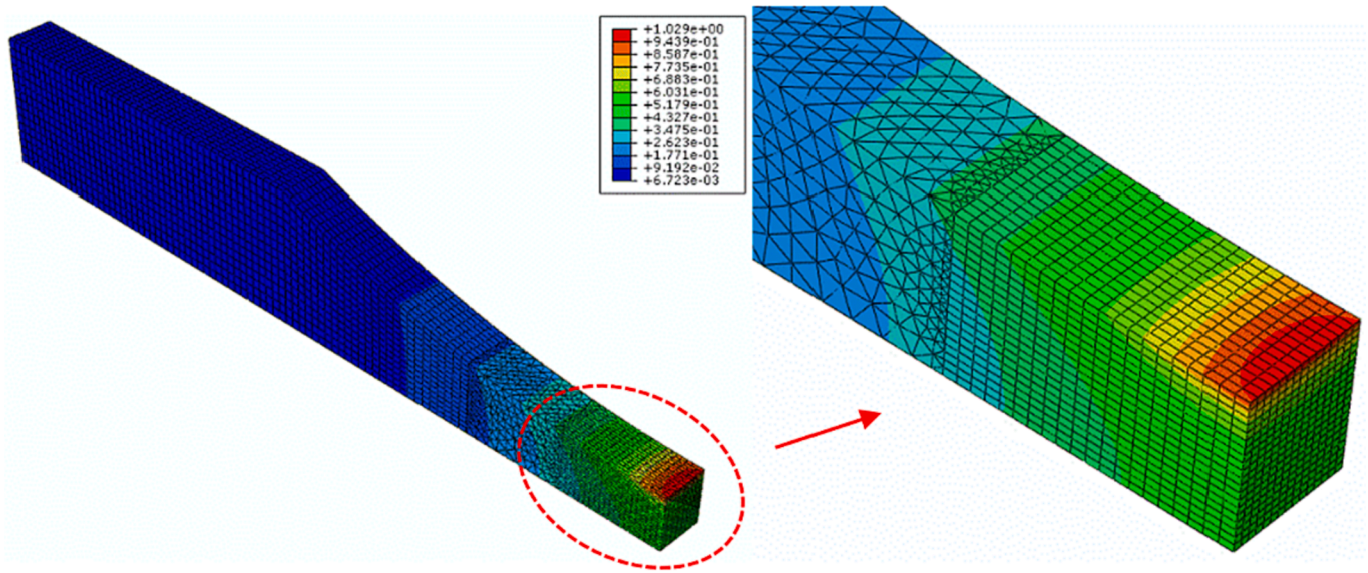


Fig. 18. Damage distribution of the ZM6 smooth specimen with $R = 0.02$ and $S_{max} = 130MPa$.

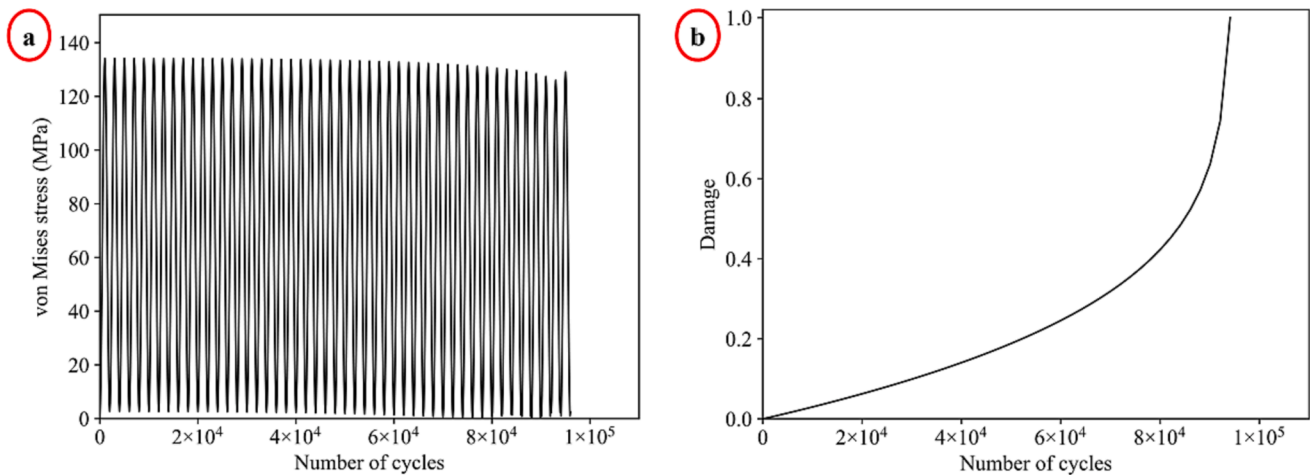


Fig. 19. For the ZM6 smooth specimen with $R = 0.02$ and $S_{max} = 130MPa$, (a) variation of von Mises stress versus the loading cycles, and (b) variation of damage versus the loading cycles.

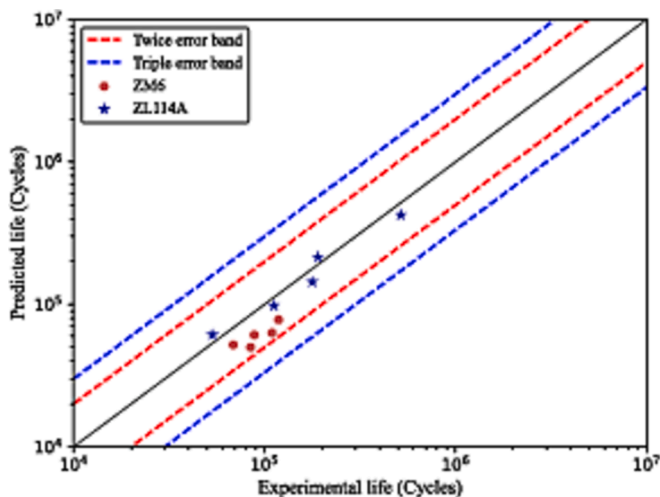


Fig. 20. The numerical predicted results versus the experimental results for the ZL114A and ZM6 smooth specimens.

experimental data of ZL114A scratched specimens. It is observed that the numerical computation results of Model-1 have a significant error, and all the data points fall outside the twice error band, indicating that the prediction accuracy is low. In contrast, the predicted results of the proposed Model-2 fall within the twice error band. The numerical computation results versus experimental data for the ZM6 scratched specimens are shown in Fig. 21(b), from which we can see that the predicted fatigue lives of Model-1 are less accurate, with only a few data falling within the triple error band and most of the data points lying outside the triple error band, while the predicted results of the proposed Model-2 agree well with the experimental data.

In terms of the specimen with pit, the variation of the experimental life of ZL114A specimens with the numerically computed data is shown in Fig. 22(a). It is clear that the prediction accuracy of both Model-1 and Model-2 is high, and most of the data fall within the twice error band. Fig. 22(b) is plotted for the predicted fatigue lives of the ZM6 specimen with pit. It is noted that most of the computed results fall within the twice error band, and only two data fall outside the triple error band.

Even though most of the results of ZL114A and ZM6 smooth and defected specimens predicted by the defect-based fatigue damage model lie within the triple error band, there is still a relative error between the

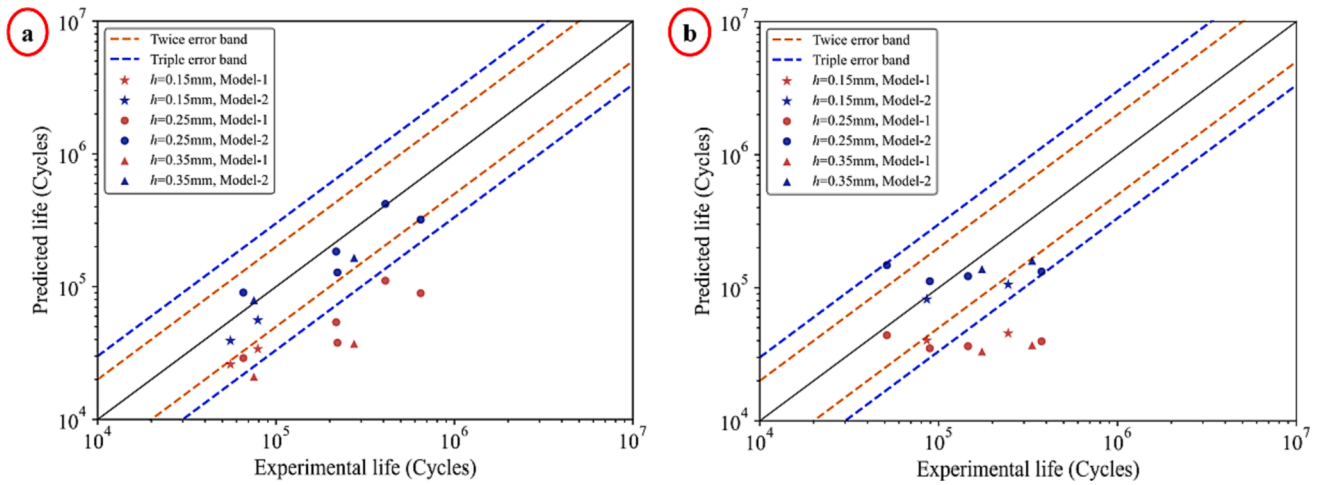


Fig. 21. Variation of predicted results with fatigue test data for the specimen with scratch: (a) ZL114A, (b) ZM6.

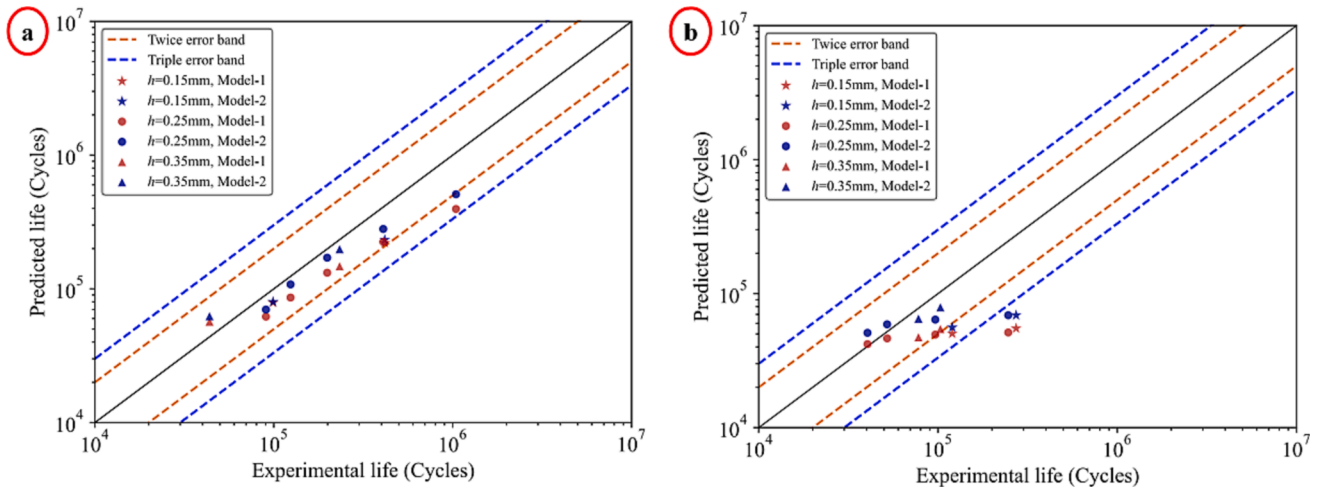


Fig. 22. Variation of predicted results with fatigue test data for the specimen with impact pit: (a) ZL114A, (b) ZM6.

predicted values and the experimental data. The following two reasons contribute to the prediction error. First, there are not sufficient experimental data. Three parameters in the defect-based fatigue damage model need to be calibrated. However, there are only five sets of experimental data. As far as probability statistics are concerned, it is known that the larger the amount of data, the more accurate the fit. Therefore, the calibration process of material parameters could cause errors. Second, the effects caused by internal pores are not considered. Studies show that porosity and the critical pores near the surface have a significant effect on the fatigue behavior of the material. The porosity characterizes the average effect of the random distribution of pores inside the material, while critical pores could induce stress concentrations near the pores, which are not taken into account in the proposed defect-based fatigue damage model.

5. Architecture of optimized neural network model

5.1. Artificial neural network

Artificial neural network (ANN) [45–46] refers to a network structure composed of numerical nodes and the computational relationships between nodes. In engineering applications, the commonly used machine learning techniques include the ANN, random forest (RF), decision tree (DT), and support vector machine (SVM). The ANN can learn on their own and produce results that are not limited by the data supplied to

them. In addition, because the input is kept in its own networks rather than a database, it does not suffer from data loss. Compared with other machine learning models, the advantages of ANN lie in the effective visual analysis, processing of unorganized data, adaptive structure, continuous learning, user-friendly interface, and so on. At the same time, due to its complex nature, the ANN model has some limitations, such as hardware dependence, black box nature, approximate results, and data dependency. A schematic diagram of ANN is shown in Fig. 23, where the circles represent neurons (numerical values), and the arrows represent links (mathematical relationships). The basic architecture of the ANN is constructed [47] by adjusting the number of hidden layers, the number of neurons in each layer, and the links between the layers.

In this study, the ANN model is employed to predict fatigue life based on the following considerations. (1) The damage model in Abaqus is computationally expensive, and it is also time-consuming to build FE models and perform numerical simulations. (2) Although the numerically computed fatigue lives are acceptable, there are still some errors compared with the experimental data. (3) We intend to develop a reliable dataset of the ANN model, including defect morphology, fatigue loads, and materials, to quickly and accurately predict the high-cycle fatigue life of casting alloys with the surface defects.

5.2. Dataset construction and data pre-processing

For the defected ZL114A and ZM6 specimens under different fatigue

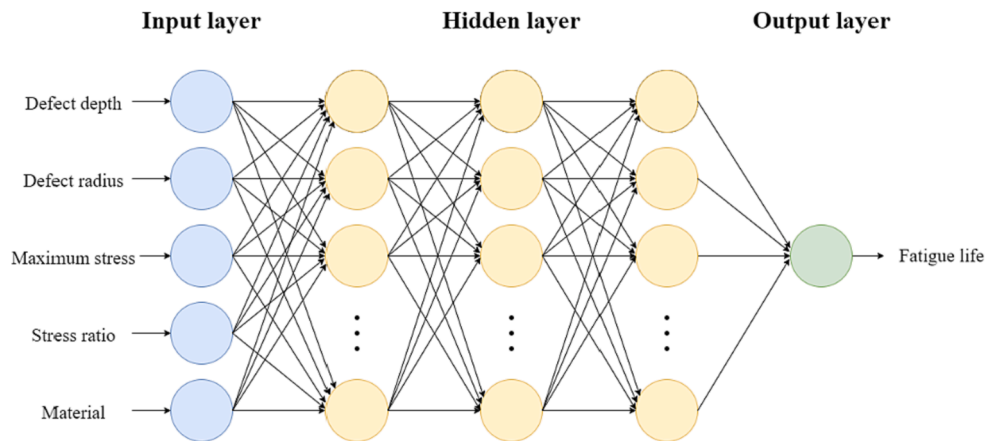


Fig. 23. A schematic diagram of ANN.

loads, 61 sets of numerical computations are performed according to the experimentally validated theoretical model and numerical method, and a batch of reliable fatigue life data is acquired. Therefore, there are 93 sets of data in the database, including 32 experimental data and 61 sets of numerically computed results.

The definitions of the input and output are presented for the ANN. It is clear that the defect morphology can be characterized by its geometric parameters, i.e. defect depth and the defect radius, while the fatigue loads can be characterized by the maximum stress and the stress ratio. Furthermore, there are two kinds of materials. Therefore, the above five parameters as inputs to the ANN can completely define the material, defects, and stress levels. Therefore, there is a corresponding relationship between these five parameters and the output fatigue life.

After that, the definitions of the training and test sets are presented for the ANN model. On the one hand, the distinction between training and test sets could help to detect the generalization of the neural network. When the ANN model is trained, the fatigue lives are directly predicted using the inputs of the training set and then compared with the experimental data. On the other hand, distinguishing between training and test sets could prevent overfitting. For the dataset of this study, 80 % of the data is employed in the network, and the remaining 20 % is used to evaluate the training results of the network.

5.3. Architecture design of the ANN model

The designed architecture of the ANN model in this study is listed in Table 5. The Dense layer is the fully connected layer, the Relu layer is the activation function layer, and Batch Normalization is the batch normalization processing layer. Each layer has a certain number of neurons, and the type of each layer represents the form of connection with the previous layer, i.e., the mathematical relationship between the two layers. The detailed workflow of the ANN model is presented as follows.

Table 5
The designed architecture of the ANN model.

Network layer	Layer type	Number of neurons
1	Input	5
2	Batch Normalization	5
3	Dense	100
4	Relu	100
5	Dense	400
6	Relu	400
7	Dense	50
8	Relu	50
9	Dense	1
10	Output	1

- (1) Model architecture design and data segmentation. The fatigue database of smooth and defected ZL114A and ZM6 specimens are imported, and the input/output and training/test data sets are split. The ANN architecture is then designed, including the number of layers, the type of layers, and the number of neurons. The loss function and optimizer are selected, and the number of training rounds is determined. After that, all the weights of the ANN model are randomly initialized.
- (2) Model training and process recording. The training set is fed into the network, and the results are computed forward. The error is then obtained based on the calculated results and the output data set. After that, the loss function and backpropagation gradient are computed based on the error, and the loss function is recorded. It is judged whether the maximum number of training rounds is reached. If not, the forward computation is performed on the test set, and the loss function is recorded.
- (3) Model test. The loss function curves are plotted based on the above computation. For the trained ANN, the forward computation is performed separately for the training/test set. The computed results are saved, and the error bands are plotted.

5.4. Model training and predicted results

The ANN model is trained for 300 rounds and then evaluated with test data. The model parameters are listed in Table 6, and the variation of the loss function with the number of training rounds is shown in Fig. 24. The red curve represents the training set, and the green curve represents the test set. It can be seen that both tend to converge as the training iteration process proceeds, where the average error of the test set is about 12.74 %, indicating the high accuracy of the ANN model. The curve of the correlation coefficient is plotted in Fig. 25, where the green data points are the training set, and the red data points represent the test set. The black dashed line is the reference line with a slope of one, meaning that the predicted results match the experimental data exactly. The solid line is the regression curve of the data points, and R_c is the correlation coefficient. The closer the value of R_c is to 1, the better the prediction is. It can be seen that the linear fit of the model is good.

After the training, the ANN model is employed to predict the fatigue life of ZL114A and ZM6 specimens under different stress levels. All the

Table 6
The parameters of the ANN model.

Number of input variables	Number of output variables	Number of training data	Number of test data	Average error
5	1	74	19	12.74 %

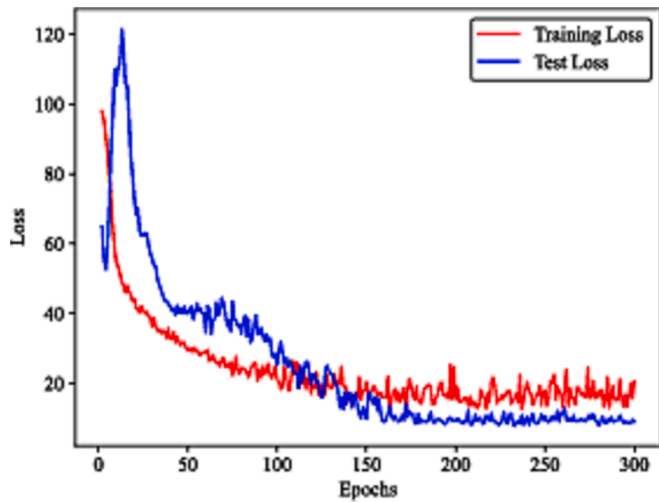


Fig. 24. Variation of loss function with the training round.

predicted results are listed in Table 7. Fig. 26 is plotted for the predicted fatigue lives, and it is observed that the prediction of the model is good, and the prediction results of the test set are within the twice error band with high accuracy.

6. Conclusion

In this work, the high-cycle fatigue behaviours of ZL114A and ZM6 alloys with the surface defects are investigated. A novel defect-based fatigue damage model coupled with an optimized neural network is proposed for fatigue life prediction. The following conclusions can be drawn from the experimental studies and numerical analysis:

- (1) Experimental studies reveal that the fatigue data dispersion of ZM6 alloy is more significant than that of ZL114A alloy, which may be related to the defects inside the specimens. It is also concluded that the casting process could induce the inclusions and holes inside the ZM6 alloy, and the size, shape, and location of the defects have important effects on the fatigue behavior, leading to a significant dispersion of experimental fatigue data.
- (2) According to finite element parametric studies, the relationship is established between the typical size of the defect and the defect impact factor (DIF), and the defect-based fatigue damage evolution equation is then derived based on the continuum damage

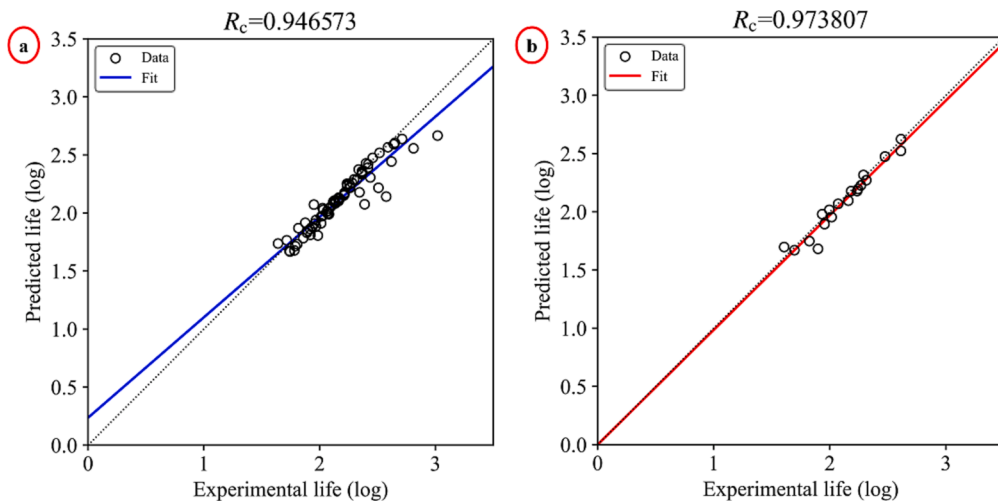


Fig. 25. The curve of correlation coefficient: (a) training set, and (b) test set.

Table 7 The predicted fatigue lives of ZL114A and ZM6 specimens.

Case No.	Material	<i>h</i>	<i>r</i>	<i>S</i> _{max}	<i>R</i>	<i>N</i> _{exp}	<i>N</i> _{pre}	Error
1	ZL114A	0.15	3	200	0.02	99,050	103,503	4.50 %
2	ZL114A	0.25	3	140	0.02	409,100	305,787	25.25 %
3	ZL114A	0.15	0.2	210	0.02	79,110	55,509	29.83 %
4	ZL114A	0.25	0.2	120	0.02	410,100	395,316	3.61 %
5	ZL114A	0.15	3	165	0.02	206,023	185,751	9.84 %
6	ZL114A	0.15	3	190	0.02	117,897	113,484	3.74 %
7	ZL114A	0.25	3	145	0.02	298,416	275,796	7.58 %
8	ZL114A	0.25	3	175	0.02	144,344	120,875	16.26 %
9	ZL114A	0.35	3	160	0.02	185,217	163,640	11.65 %
10	ZL114A	0.35	3	185	0.02	103,655	80,785	22.06 %
11	ZL114A	0.15	0.2	225	0.02	49,551	51,198	3.32 %
12	ZL114A	0.25	0.2	155	0.02	194,753	200,270	2.83 %
13	ZL114A	0.35	0.2	160	0.02	152,493	138,914	-8.91 %
14	ZM6	0.25	3	134	0.02	40,418	46,291	14.53 %
15	ZM6	0.15	0.2	120	0.02	85,894	97,846	13.91 %
16	ZM6	0.25	0.2	92	0.02	174,636	171,583	1.75 %
17	ZM6	0.25	3	128	0.02	66,628	54,889	17.62 %
18	ZM6	0.35	3	112	0.02	90,060	82,890	7.96 %
19	ZM6	0.25	0.2	94	0.02	171,888	163,795	4.71 %

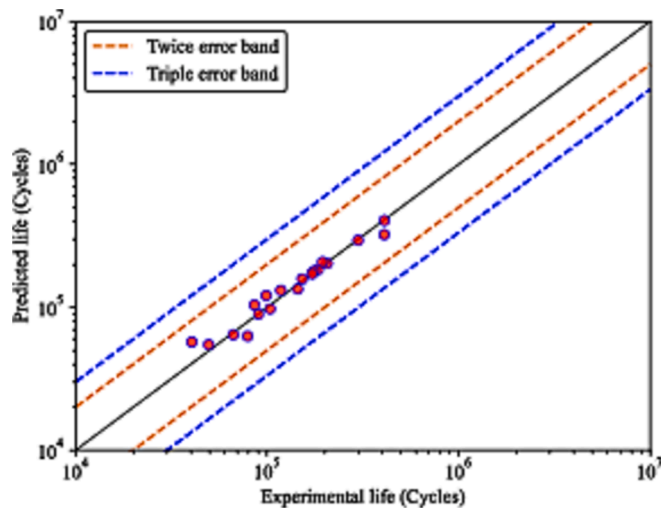


Fig. 26. Variation of the predicted results with fatigue test data.

mechanics. Finally, the calibration of material parameters is carried out.

- (3) The numerical simulations and fatigue damage computations of ZL114A and ZM6 specimens are implemented, and the effectiveness of the proposed theoretical model is validated. More numerical computations are then performed to obtain a batch of reliable fatigue data, which forms the database of the artificial neural network model.
- (4) The architecture of the optimized neural network model is established, the model training is conducted, and the predicted results are obtained, which are verified by the experimental fatigue data of ZL114A and ZM6 specimens.
- (5) Outlook for future research. Future work is needed to further develop the proposed defect-based fatigue damage model to take into account internal defects (including microstructures, porosity, and inclusions). Although the numerically computed fatigue lives are within the acceptable error range compared with experimental data, the prediction accuracy can still be improved by refining the theoretical model. Furthermore, the applicability of the optimized neural network model needs to be further explored, and other metallic materials, as well as other types of defects, need to be investigated.

Declaration of Competing Interest

The authors declare that they have no known competing financial interests or personal relationships that could have appeared to influence the work reported in this paper.

Data availability

Data will be made available on request.

Acknowledgement

Zhixin Zhan sincerely acknowledges the support from the National Natural Science Foundation of China (No. 12002011), the Fundamental Research Funds for the Central Universities and the Opening fund of State Key Laboratory of Nonlinear Mechanics. Chuanqi Liu is supported by the One Hundred Talents Program of the Chinese Academy of Sciences and National Natural Science Foundation of China (No. 12172368).

References

- [1] Luo P, Yao W, Li P. A notch critical plane approach of multiaxial fatigue life prediction for metallic notched specimens. *Fatigue Fract Eng Mater Struct* 2019;42(4):854–70.
- [2] Luo P, Yao W, Susmel L, et al. Prediction of fatigue damage region with the use of the notch critical plane approach for crack initiation and propagation. *Int J Fatigue* 2020;135:105533.
- [3] Li J, Wang X, Li R, et al. Multiaxial fatigue life prediction for metals by means of an improved strain energy density-based critical plane criterion. *European Journal of Mechanics-A/Solids* 2021;90:104353.
- [4] Benedetti M, Berto F, Le Bone L, et al. A novel Strain-Energy-Density based fatigue criterion accounting for mean stress and plasticity effects on the medium-to-high-cycle uniaxial fatigue strength of plain and notched components. *Int J Fatigue* 2020;133:105397.
- [5] Sharma D, Pandey VB, Singh IV, et al. A polygonal FEM and continuum damage mechanics based framework for stochastic simulation of fatigue life scatter in duplex microstructure titanium alloys. *Mech Mater* 2021;163:104071.
- [6] Huang J, Meng Q, Zhan Z, et al. Damage mechanics-based approach to studying effects of overload on fatigue life of notched specimens. *Int J Damage Mech* 2019;28(4):538–65.
- [7] Corigliano P, Crupi V, Pei X, et al. DIC-based structural strain approach for low-cycle fatigue assessment of AA 5083 welded joints. *Theor Appl Fract Mech* 2021;116:103090.
- [8] Ren X, Xu X, Jiang C, et al. Strain distribution and fatigue life estimation for steel plate weld joint low cycle fatigue based on DIC. *Opt Lasers Eng* 2020;124:105839.
- [9] Liao D, Zhu SP, Keshtegar B, et al. Probabilistic framework for fatigue life assessment of notched components under size effects. *Int J Mech Sci* 2020;181:105685.
- [10] Lythakula KR, Yuan FG. A probabilistic fatigue life prediction for adhesively bonded joints via anns-based hybrid model. *Int J Fatigue* 2021;151:106352.
- [11] Yasbolaghi R, Khoei AR. Micro-structural aspects of fatigue crack propagation in atomistic-scale via the molecular dynamics analysis. *Eng Fract Mech* 2020;226:106848.
- [12] Akbarian S, Dehghani K. On the molecular dynamics simulation of fatigue behavior of pre-cracked aluminum chip for NEMS application: Effect of cyclic loading mode and surface roughness geometry. *Int J Fatigue* 2020;135:105570.
- [13] Loew PJ, Peters B, Beex LAA. Fatigue phase-field damage modeling of rubber using viscous dissipation: Crack nucleation and propagation. *Mech Mater* 2020;142:103282.
- [14] Simoes M, Martínez-Pañeda E. Phase field modelling of fracture and fatigue in Shape Memory Alloys. *Comput Methods Appl Mech Eng* 2021;373:113504.
- [15] Liu B, Bao R, Sui F. A fatigue damage-cumulative model in peridynamics. *Chin J Aeronaut* 2021;34(2):329–42.
- [16] Nguyen CT, Oterkus S, Oterkus E. An energy-based peridynamic model for fatigue cracking. *Eng Fract Mech* 2021;241:107373.
- [17] Peng X, Wu S, Qian W, et al. The potency of defects on fatigue of additively manufactured metals. *Int J Mech Sci* 2022;221:107185.
- [18] Yang J, Kang G, Kan Q. Rate-dependent multiaxial life prediction for polyamide-6 considering ratchetting: Semi-empirical and physics-informed machine learning models. *Int J Fatigue* 2022;163:107086.
- [19] Couper MJ, Neeson AE, Griffiths JR. Casting defects and the fatigue behaviour of an aluminium casting alloy. *Fatigue Fract Eng Mater Struct* 1990;13(3):213–27.
- [20] Avalle M, Belingardi G, Cavatorta MP, et al. Casting defects and fatigue strength of a die cast aluminium alloy: a comparison between standard specimens and production components. *Int J Fatigue* 2002;24(1):1–9.
- [21] Serrano-Munoz I, Buffiere JY, Verdu C, et al. Influence of surface and internal casting defects on the fatigue behaviour of A357-T6 cast aluminium alloy. *Int J Fatigue* 2016;82:361–70.
- [22] Mayer H, Papakyriacou M, Zettl B, et al. Influence of porosity on the fatigue limit of die cast magnesium and aluminium alloys. *Int J Fatigue* 2003;25(3):245–56.
- [23] Yi JZ, Gao YX, Lee PD, et al. Scatter in fatigue life due to effects of porosity in cast A356-T6 aluminum-silicon alloys. *Metall Mater Trans A* 2003;34(9):1879–90.
- [24] Buffiere JY, Savelli S, Jouneau PH, et al. Experimental study of porosity and its relation to fatigue mechanisms of model Al-Si7-Mg0. 3 cast Al alloys. *Mater Sci Eng A* 2001;316(1–2):115–26.
- [25] Siegfanz S, Gertler A, Michels W, et al. Influence of the microstructure on the fatigue damage behaviour of the aluminium cast alloy AlSi7Mg0. 3. *Mater Sci Eng A* 2013;565:21–6.
- [26] Ge B, Liu X, He G, et al. Quantitative relationship between microstructure characteristics and fatigue parameters of A319 casting alloy. *Fatigue Fract Eng Mater Struct* 2020;43(3):605–16.
- [27] He L, Wang Z, Ogawa Y, et al. Machine-learning-based investigation into the effect of defect/inclusion on fatigue behavior in steels[J]. *Int J Fatigue* 2022;155:106597.
- [28] Salvati E, Tognan A, Laurenti L, et al. A defect-based physics-informed machine learning framework for fatigue finite life prediction in additive manufacturing[J]. *Mater Des* 2022;222:111089.
- [29] Li A, Baig S, Liu J, et al. Defect Criticality Analysis on Fatigue Life of L-PBF 17–4 PH Stainless Steel via Machine Learning[J]. *Int J Fatigue* 2022;107018.
- [30] Zhan Z, Ao N, Hu Y, et al. Defect-induced fatigue scattering and assessment of additively manufactured 300M-AerMet100 steel: An investigation based on experiments and machine learning[J]. *Eng Fract Mech* 2022;264:108352.
- [31] Tan L, Yang XG, Shi DQ, et al. Unified fatigue life modelling and uncertainty estimation of Ni-based superalloy family with a supervised machine learning approach[J]. *Eng Fract Mech* 2022;275:108813.

- [32] Fernández J, Chiachío M, Chiachío J, et al. Uncertainty quantification in Neural Networks by Approximate Bayesian Computation: Application to fatigue in composite materials[J]. *Eng Appl Artif Intel* 2022;107:104511.
- [33] Heng J, Zheng K, Feng X, et al. Machine Learning-Assisted probabilistic fatigue evaluation of Rib-to-Deck joints in orthotropic steel decks[J]. *Eng Struct* 2022;265:114496.
- [34] Gu HH, Wang RZ, Zhu SP, et al. Machine learning assisted probabilistic creep-fatigue damage assessment[J]. *Int J Fatigue* 2022;156:106677.
- [35] Li J, Yang Z, Qian G, et al. Machine learning based very-high-cycle fatigue life prediction of Ti-6Al-4V alloy fabricated by selective laser melting[J]. *Int J Fatigue* 2022;158:106764.
- [36] Maleki E, Bagherifard S, Razavi SMJ, et al. On the efficiency of machine learning for fatigue assessment of post-processed additively manufactured AlSi10Mg[J]. *Int J Fatigue* 2022;160:106841.
- [37] Doh J, Raju N, Raghavan N, et al. Bayesian inference-based decision of fatigue life model for metal additive manufacturing considering effects of build orientation and post-processing[J]. *Int J Fatigue* 2022;155:106535.
- [38] Dang L, He X, Tang D, et al. A fatigue life prediction approach for laser-directed energy deposition titanium alloys by using support vector regression based on pore-induced failures[J]. *Int J Fatigue* 2022;159:106748.
- [39] HB 5287-96, Test method for axial loading fatigue of metallic materials, Aviation Industry Corporation of China, 1996.
- [40] Yang S, Hu W, Zhan Z, et al. Fatigue tests and a damage mechanics-based fatigue model on a cast Al-Si-Mg aluminum alloy with scratches. *Int J Fatigue* 2022;165:107198.
- [41] Murakami S. Continuum damage mechanics: a continuum mechanics approach to the analysis of damage and fracture. Springer Science & Business Media; 2012.
- [42] Gao T, Tong Y, Zhan Z, et al. Development of a non-local approach for life prediction of notched specimen considering stress/strain gradient and elastic-plastic fatigue damage. *Int J Damage Mech* 2022:10567895221089663.
- [43] Liu N, Cui X, Xiao J, et al. A simplified continuum damage mechanics based modeling strategy for cumulative fatigue damage assessment of metallic bolted joints. *Int J Fatigue* 2020;131:105302.
- [44] Shen F, Zhao B, Li L, et al. Fatigue damage evolution and lifetime prediction of welded joints with the consideration of residual stresses and porosity. *Int J Fatigue* 2017;103:272-9.
- [45] Nejad RM, Sina N, Ma W, et al. Optimization of fatigue life of pearlitic Grade 900A steel based on the combination of genetic algorithm and artificial neural network. *Int J Fatigue* 2022;162:106975.
- [46] Farid M. Data-driven method for real-time prediction and uncertainty quantification of fatigue failure under stochastic loading using artificial neural networks and Gaussian process regression. *Int J Fatigue* 2022;155:106415.
- [47] Liu S, Shi W, Zhan Z, et al. On the development of error-trained BP-ANN technique with CDM model for the HCF life prediction of aluminum alloy. *Int J Fatigue* 2022;160:106836.